Article:
Li, B., Chen, M., Yu, G. et al. (2025) Robust real-time energy management of flexible traction substation with energy storage and PV for heavy-haul railways. Control Engineering Practice, 165. 106558. ISSN: 0967-0661

https://doi.org/10.1016/j.conengprac.2025.106558

Robust Real-Time Energy Management of Flexible Traction Substation With Energy Storage and PV for Heavy-Haul Railways

Bo Li[a,b], Minwu Chen[a,*], Guowang Yu[c], Chen Chen[b], Yinyu Chen[a] and Kang Li[d]

[a]School of Electrical Engineering, Southwest Jiaotong University, Chengdu 611756, China
[b]Electrification & Telegraphy Engineering Design Research Department, China Railway Design Corporation, Tianjin 300308, China
[c]CHN Energy Shuohuang Railway Development Co., Ltd., Cangzhou, 062350, China
[d]School of Electronic and Electrical Engineering, University of Leeds, Leeds, LS2 9JT, UK

ARTICLE INFO

Keywords:
real-time energy management
robust optimization
model-free predictive control
heavy-haul railway
uncertainty

ABSTRACT

Flexible traction substation (F-TSS), comprising a power flow controller (PFC), energy storage system (ES), and photovoltaic (PV) system, serves as a critical energy nexus for heavy-haul railways. However, the stochastic nature of heavy-duty electric locomotives and PVs poses significant challenges to ensuring the safe and efficient operation of the railway system. Correspondingly, a real-time energy management system framework (R-EMS) is constructed in this paper. At the R-EMS optimization stage, a day-ahead robust optimization approach is introduced to handle worst-case scenarios, ensuring the resilient operation of the F-TSS under uncertainties in freight train power and PV output while maximizing energy savings. At the R-EMS control stage, a direct-type Model-Free Adaptive Predictive Control method with error differential characteristics (ED-dMFAPC) is proposed to enable rapid and precise tracking of day-ahead scheduling plans for the PFC and ES. This method features a simple incremental structure, equivalent to an ideal predictive controller, and incorporates a compensation strategy to mitigate voltage imbalance and support reactive power in real-time. These two stages operate sequentially on day-ahead and intra-day timescales, effectively balancing robustness and economic performance. Simulation-based comparative studies, built on realistic FTPS configurations, are conducted to evaluate the proposed strategy, achieving a 13.39 % reduction in costs and a significant improvement in the Integral of Squared Error (ISE) and Integral of Absolute Error (IAE), with reductions of at least 89 %.

1. Introduction

Heavy-haul railways are recognized as the most energy-efficient mode of land-based transportation for bulk commodities. For instance, over 60 % of China's total coal freight and 40 % of America's long-haul freight are transported by heavy-haul railways. Guided by the shared vision of Heavy Haul 4.0, released by the International Heavy Haul Association in 2018 [1], Flexible Traction Power Systems (FTPSs) are expected to play a crucial role in the electrification of freight railways. The widespread adoption of FTPSs can enhance the energy efficiency and environmental sustainability of heavy-haul railways, facilitate the high utilization of regenerative braking energy (RBE), and improve the efficiency and robustness of photovoltaic (PV) systems [2].

To improve the performance of FTPSs in RBE recovery and operational cost reduction, energy management has become a key research focus in heavy-haul railways. Existing energy-saving strategies primarily fall into three categories: (1) Energy-efficient control of electric locomotives. Tao *et al.* [3] proposed a joint optimization strategy for energy saving and voltage stability in multi-train operations. Xiao *et al.* [4] developed a vehicle-line-coupled dynamics model to minimize energy consumption through cooperative train control. Unified train trajectory optimization methods have also been studied by Tian *et al.* [5] and Cao *et al.* [6]. (2) Electrification alternatives for diesel locomotives, including battery-electric and hydrogen-powered trains. Xiao *et al.* [7] formulated an integrated source-catenary-load-storage optimization model to capture the coupling between hybrid trams and power infrastructure. Popovich *et al.* [8] discussed the technical and economic feasibility of battery-electric trains. Deng *et al.* [9] applied Pontryagin's Minimum Principle to design an adaptive energy management strategy for fuel cell hybrid trains, aiming at zero-emission operations. (3) Collaborative optimization of train scheduling and regenerative energy usage. Previous studies often assume that regenerative energy from braking trains can be absorbed simultaneously by accelerating ones [3]. However, our earlier work [10] indicated that overlooking the interaction between trains and the traction power supply system can lead to substantial RBE waste. This reveals the limitation of train-level optimization in achieving system-wide energy efficiency and highlights the need to consider FTPS-level coordination.

The traction substation (TSS), integrated with a traction transformer, power flow controllers (PFCs), energy storage systems (ESSs), and distributed PVs, serves as the energy hub of heavy-haul railway systems, as illustrated in Fig. 1. It enables bidirectional power exchange between the main power grid and the heavy-duty electric locomotive loads. Recently, a variety of TSS energy management strategies have garnered widespread attention. Aguado *et al.* [11] proposed energy management models focused on energy storage, while Novak *et al.* [12] developed a model predictive control framework for TSS using a hierarchical structure.

*Minwu Chen, chenminwu@home.swjtu.edu.cn

Dong *et al.* [13] further introduced a coordinated control strategy for multi-source traction systems integrated with both ES and PV. However, these studies are predominantly based on deterministic power flow predictions, without accounting for the inherent prediction errors encountered in practice. In reality, power flow arising from the interaction between the electrical network and trains, as well as PV output, is subject to uncertainty due to variable driving behaviors and stochastic weather conditions [14].stochastic climate changes [14].

To address the challenge of uncertainty in energy management, both stochastic optimization and robust optimization (RO) have been widely applied, each offering distinct advantages depending on the nature of uncertainty. Wang *et al.* [15] proposed a dispatch method based on conditional value-at-risk (CVaR) and probabilistic scenarios, while Chen *et al.* [16] introduced a chance-constrained two-stage programming method to determine the size of PFC and ES systems. Jiang *et al.* [17] and Kumar *et al.* [18] proposed a multi-timescale energy management framework to address multi-source uncertainties. These scenario- or chance-constrained based approaches aim to capture uncertainties in PV output and traction load, but they may still lead to violations of operational constraints or suboptimal decisions under extreme conditions. In contrast, robust optimization offers a more conservative yet reliable solution by optimizing for the worst-case scenario within a predefined uncertainty set, thus ensuring feasibility across all realizations of uncertainty. Despite its advantages, research on robust energy management in TSS is still limited. Liu *et al.* [19] developed a two-stage robust optimization model to improve both the reliability and economic performance of flexible TSS operations. However, most existing studies, including [11]–[19], focus on day-ahead scheduling and fail to incorporate uncertainties in real-time or intraday operations. Consequently, TSS operators are often constrained to follow predetermined day-ahead schedules, lacking the flexibility to adapt to real-time deviations caused by volatile PV generation or fluctuating train loads. Moreover, stochastic approaches require accurate probabilistic models of uncertainties—information that is often difficult to obtain in practice.

Deployment of real-time energy management processes has been a vogue in recent research trends. Ge *et al.* [20] designed a real-time hierarchical energy management strategy to maximize the RBE and PV energy utilization. Various advanced droop controllers are constructed to enhance the flexibility and reliability of the FTPS by Guo *et al.* [21] and Wang *et al.* [22]. Guo *et al.* [23] proposed a multi-timescale energy management strategy including the minutes-level optimal dispatch for main-TSS and the seconds-level real-time control for sub-TSS. Consequently, real-time dispatch problems are often formulated as multi-layer control strategies [20]-[22] or multi-time control models [23]. However, due to the substantial fluctuations in traction power demand, ensuring robustness remains a critical requirement. This necessitates not only the formulation of an upper-layer robust optimization model to handle worst-case scenarios, but also the design of a lower-layer real-time control strategy with fast dynamic response to accurately track dispatch targets and maintain stable operation.

In the FTPSs, the interaction between heavy-haul locomotives, PFCs, and energy storage systems introduces considerable nonlinearity and time-varying behaviour, particularly when translating day-ahead scheduling decisions into real-time control actions [14]. These rapid operational changes alter the internal parameters of the system, thereby affecting its dynamic response characteristics. Conventional Proportional–Integral–Derivative (PID) controllers, which rely on fixed linear models, often struggle to maintain performance and robustness in the presence of these nonlinearities and uncertainties [24]. Although PID-based control is widely adopted due to its simplicity and ease of implementation, it lacks adaptability to changing environments. When applied in such scenarios, it may result in degraded power quality, voltage oscillations, or even emergency shutdowns [22, 23].

To cope with these challenges, recent research has explored data-driven control approaches that can learn system dynamics directly from operational data, without requiring detailed physical models [25, 26]. Among these, model-free adaptive predictive control (MFAPC) has emerged as a promising method. It builds dynamic data models in real time and adjusts control actions based on real-time input–output data, thus offering enhanced flexibility and tracking accuracy. MFAPC has shown effectiveness in managing nonlinear control problems in power electronic and grid-interactive systems [27, 28, 29]. However, the application of MFAPC in railway traction systems introduces a key distinction from grid-based control tasks: in addition to tracking the scheduled power flow, the real-time controller must also compensate for power quality issues such as voltage unbalance and low power factor, which are more pronounced in heavy-haul railway environments due to the single-phase nature and high variability of traction loads. To the best of our knowledge, no prior work has investigated the integration of MFAPC with real-time power quality compensation for railway traction energy management systems.

Given the identified research gaps, this study is the first to explore a robust real-time dispatch model for the F-TSS of heavy-haul railways, addressing the stochastic nature of freight train power demand and PV output. The key contributions of this paper are summarised as follows:

- A real-time energy management system (R-EMS) framework is developed for FTPSs in heavy-haul railways, integrating minute-level economic dispatch with second-level power quality regulation.
- A robust R-EMS optimization method is proposed to coordinate PFC and energy storage (ES) facilities in FTPSs, aiming to mitigate worst-case uncertainty while minimizing operational costs. This method addresses the uncertainties associated with freight train

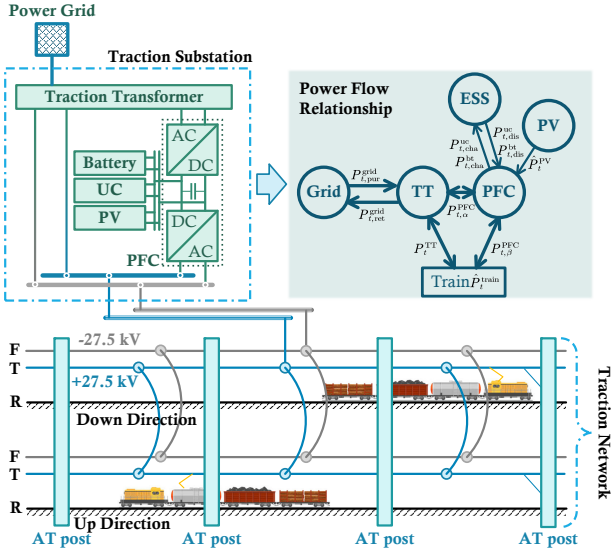

Figure 1: Configuration of Traction Power System for Heavy-haul railway.

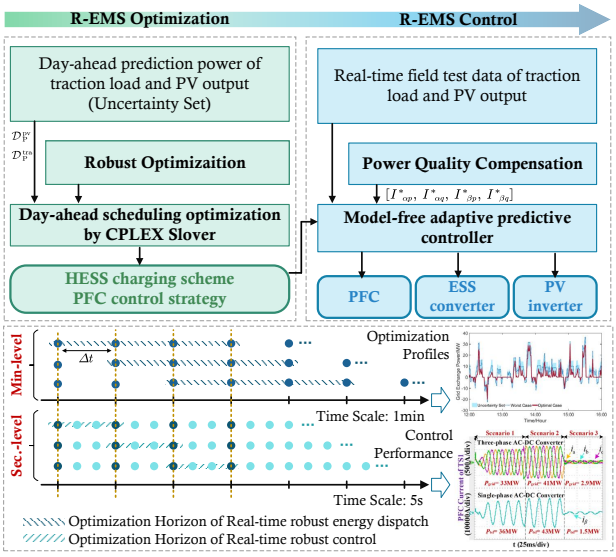

Figure 2: Real-time Energy Management Framework.

power demand and PV output using a two-stage robust optimization (RO) approach.

- To address the most critical power quality issue in heavy-haul railways—voltage unbalance—a voltage regulation and power factor compensation model is embedded into the R-EMS control strategy. The proposed scheme enables real-time mitigation of voltage and reactive power fluctuations induced by single-phase freight train operation.

- To enhance the dynamic performance of real-time R-EMS control and suppress the effects of power disturbances in converter systems, a direct-type model-free adaptive predictive control (dMFAPC) method is developed. This approach simplifies controller design by formulating it as a parameter optimization problem without significantly increasing computational complexity.

The rest of this paper is organised as follows. Section 2 introduces the proposed F-TSS and its energy management framework. Section 3 presents the R-EMS optimization approach. Section 4 provides the converter control schemes with dMFAPC. Section 6 reports case studies and their results. Section 7 draws the conclusions.

2. Architecture for Flexible TSS and Energy Management

2.1. Topology of Flexible TSS Configuration

Fig. 1 shows the configuration of TPS including flexible TSS and 2×25 kV traction networks. As shown, the TSS consists of a PFC and an AC traction transformer (TT), which can provide continuous power with the same voltage amplitude and phase to the train. The TT has a special balance connection, such as Scott-connected or Ynvd-connected, when energy flowing through the PFC side is equal on the other side, the voltage unbalance (VU) will be naturally eliminated in the three-phase grid side. Meanwhile, the hybrid energy storage system (HESS), including batteries and ultracapacitors (UCs), is connected to the PFC's DClink, which can absorb/generate RBE to reduce the peak and fill the valley. The batteries have high energy density and are suitable for storing large amounts of energy. In contrast, UC is more ideal as a fast response device to reduce the negative impact of drastic changes in traction load on batteries and the power grid. Moreover, PV is introduced to partially provide energy to trains and HESS.

Traction networks in the proposed system are a network of overhead wires used to supply electric power to trains. This system consists of contact wire (C), line feeder wire (F) and rail (R), which trains connect to via pantographs, allowing them to draw the necessary electricity for propulsion. Moreover, an autotransformer (AT) post refers to a specific location within a heavy-haul railway system where an AT is situated, which is used to adjust voltage levels and enhance transmission power capacity within the traction network.

2.2. Robust Real-Time Energy Management Framework

In order to reduce the operation costs and improve the robustness of the control system, the architecture of the R-EMS is illustrated in Fig. 2. It can be seen that the framework conducted R-EMS optimization and R-EMS control on different time scales. At the R-EMS optimization stage, the traction load and PV output power take their forecast value and are then converted into an uncertainty set, to obtain an economic operation schedule against the worst scenario on a minute scales, the PFC control strategies and HESS charging/discharging schemes are determined by formulating a robust optimization model. At the R-EMS control stage, to eliminate the operation deviation between the baseline power and real-time power flow, while mitigating the VU and improve the power factor (PF), the charge and discharge

state of HESS and the power flow direction of PFC will be adjusted by the model-free APC within the moved time window.

3. R-EMS Optimization: Robust Energy Dispatch

3.1. RO Problem Statement

The RO model for the TSS operation is formulated as a typical three-level Min-Max-Min problem, as shown in Problem 3.1. The outer minimization problem ($\min_{\boldsymbol{x}}$) seeks to determine the optimal first-stage strategies, including HESS charge/discharge and energy transactions, in preparation for potential uncertainties while minimizing operational cost. Given a first-stage decision $\boldsymbol{x}$, the middle-layer maximization problem ($\max_{\boldsymbol{u}\in\mathcal{D}_{\mathrm{P}}}$) identifies the worst-case realisation of uncertain parameters—traction power demand and PV output—within the polyhedral uncertainty set $\mathcal{D}_{\mathrm{P}}$. Then, the inner-layer minimization problem ($\min_{\boldsymbol{y}\in\Omega(x,u)}$) determines the second-stage control decisions $\boldsymbol{y}$ that minimize the cost under given (x, u), subject to operational and power balance constraints. These constraints—covering power flow equations, device limits, and coupling relationships—are collectively represented by the feasible region $\Omega(x, u)$, which is further detailed in Section 3.1.2.

Problem 3.1 (Robust Optimization Problem)**.**

$$\mathcal{J}_o = \min_{\boldsymbol{x}} \left\{ \max_{\boldsymbol{u}\in\mathcal{D}_{\mathrm{P}}} \min_{\boldsymbol{y}\in\Omega(\boldsymbol{x},\boldsymbol{u})} \boldsymbol{\omega}^{\top}\boldsymbol{y} \mid \boldsymbol{A}\boldsymbol{x} \leqslant \boldsymbol{f} - \boldsymbol{D}\boldsymbol{y} \right\}$$

$$\text{s.t.} \quad \boldsymbol{x} \in \{0,1\},\ \boldsymbol{u}_{\mathrm{tra}} \in \mathcal{D}_{\mathrm{P}}^{\mathrm{tra}},\ \boldsymbol{u}_{\mathrm{pv}} \in \mathcal{D}_{\mathrm{P}}^{\mathrm{pv}}$$

$$\Omega(\boldsymbol{x},\boldsymbol{u}) = \left\{ \boldsymbol{y} \;\middle|\; \begin{array}{l} \boldsymbol{A}\boldsymbol{x} + \boldsymbol{D}\boldsymbol{y} \leqslant \boldsymbol{f} \\ \boldsymbol{B}\boldsymbol{y} \leqslant \boldsymbol{g} \\ \boldsymbol{E}\boldsymbol{y} = \boldsymbol{d} \\ \boldsymbol{G}\boldsymbol{y} = \boldsymbol{u}_{\mathrm{tra}} \\ \boldsymbol{I}\boldsymbol{y} \leqslant \boldsymbol{u}_{\mathrm{pv}} \end{array} \right\}$$

where $\boldsymbol{x}$ denotes the vector of binary variables including κ_t^{grid}, κ_t^{bt} and κ_t^{uc} in the first-stage, and $\boldsymbol{y}$ represents the vector of continuous variables including $P_{t,\alpha}^{\mathrm{PFC}}$, $P_{t,\beta}^{\mathrm{PFC}}$, $P_{t,\mathrm{dis}}^{\mathrm{bt}}$, $P_{t,\mathrm{cha}}^{\mathrm{bt}}$, $P_{t,\mathrm{dis}}^{\mathrm{uc}}$, $P_{t,\mathrm{cha}}^{\mathrm{uc}}$, $P_{t,\mathrm{pur}}^{\mathrm{grid}}$, $P_{t,\mathrm{ret}}^{\mathrm{grid}}$ and P_t^{TT} in the second-stage. Moreover, $\boldsymbol{A}$, $\boldsymbol{B}$, $\boldsymbol{D}$, $\boldsymbol{E}$, $\boldsymbol{G}$, $\boldsymbol{I}$, $\boldsymbol{f}$, $\boldsymbol{g}$ and $\boldsymbol{d}$ are coefficient matrices and vectors.

3.1.1. Objective Function

The objective function consists of three terms: energy consumption cost (C^{ene}), demand cost (C^{dem}) and HESS degradation cost (C^{es}). The optimization problem aims to find the optimal control actions $(\boldsymbol{x}, \boldsymbol{y})$ under the expected robustness parameters (Γ^{tra}, Γ^{pv}). When an optimal solution is found, there is no incentive to increase or decrease the value of Γ because either action will deteriorate the objective function.

$$\boldsymbol{\omega}^{\top}\boldsymbol{y} = C^{\mathrm{ene}} + C^{\mathrm{dem}} + C^{\mathrm{es}} \tag{1}$$

where

$$C^{\mathrm{ene}} = \sum_{t=1}^{\mathrm{T}} \omega^{\mathrm{buy}} P_{\mathrm{buy},t}^{\mathrm{grid}} \Delta t \tag{2a}$$

$$C^{\mathrm{dem}} = \omega^{\mathrm{dem}} P_{\mathrm{dem},t}^{\mathrm{grid\,max}} \quad \forall t = 1, 2, \cdots, \mathrm{T}-14 \tag{2b}$$

$$C^{\mathrm{es}} = \sum_{t=1}^{\mathrm{T}} \omega^{\mathrm{bt}} \left(P_{\mathrm{cha},t}^{\mathrm{bt}} + P_{\mathrm{dis},t}^{\mathrm{bt}} \right) + \omega^{\mathrm{uc}} \left(P_{\mathrm{cha},t}^{\mathrm{uc}} + P_{\mathrm{dis},t}^{\mathrm{uc}} \right) \tag{2c}$$

Here, $P_{\mathrm{buy},t}^{\mathrm{grid}}$ and ω^{buy} represent the active power supplied by the utility grid and the cost of purchased electricity, respectively. $P_{\mathrm{dem},t}^{\mathrm{grid\,max}}$ and ω^{dem} represent the maximum peak demand power and its electricity cost, respectively. T is the total number of time intervals for scheduling during a day.

3.1.2. Constraints

To focus on the RO issue, the constraints are formulated as deterministic ones. They are listed as follows.

$$P_{t,\alpha}^{\mathrm{PFC}} + P_{t,\mathrm{dis}}^{\mathrm{bt}} + P_{t,\mathrm{dis}}^{\mathrm{uc}} + \hat{P}_t^{\mathrm{PV}} = P_{t,\beta}^{\mathrm{PFC}} + P_{t,\mathrm{cha}}^{\mathrm{bt}} + P_{t,\mathrm{cha}}^{\mathrm{uc}} \tag{3}$$

$$P_t^{\mathrm{TT}} + P_{t,\alpha}^{\mathrm{PFC}} = P_{t,\mathrm{pur}}^{\mathrm{grid}} - P_{t,\mathrm{ret}}^{\mathrm{grid}} \tag{4}$$

$$P_t^{\mathrm{TT}} + P_{t,\beta}^{\mathrm{PFC}} = \hat{P}_t^{\mathrm{train}} \tag{5}$$

$$E_t^{\mathrm{bt}} - E_{t-1}^{\mathrm{bt}} = \eta_{\mathrm{cha}}^{\mathrm{bt}} P_{t,\mathrm{cha}}^{\mathrm{bt}} \Delta t - \frac{1}{\eta_{\mathrm{dis}}^{\mathrm{bt}}} P_{t,\mathrm{dis}}^{\mathrm{bt}} \Delta t \tag{6}$$

$$E_t^{\mathrm{uc}} - E_{t-1}^{\mathrm{uc}} = \eta_{\mathrm{cha}}^{\mathrm{uc}} P_{t,\mathrm{cha}}^{\mathrm{uc}} \Delta t - \frac{1}{\eta_{\mathrm{dis}}^{\mathrm{uc}}} P_{t,\mathrm{dis}}^{\mathrm{uc}} \Delta t \tag{7}$$

$$E_{\min}^{\mathrm{bt}} \leqslant E_t^{\mathrm{bt}} \leqslant E_{\max}^{\mathrm{bt}} \tag{8}$$

$$E_{\min}^{\mathrm{uc}} \leqslant E_t^{\mathrm{uc}} \leqslant E_{\max}^{\mathrm{uc}} \tag{9}$$

$$E_{t=1}^{\mathrm{bt}} = E_{t=\mathrm{T}}^{\mathrm{bt}} = E_{\mathrm{ini}}^{\mathrm{bt}} \tag{10}$$

$$E_{t=1}^{\mathrm{uc}} = E_{t=\mathrm{T}}^{\mathrm{uc}} = E_{\mathrm{ini}}^{\mathrm{uc}} \tag{11}$$

$$0 \leqslant P_{\mathrm{buy},t}^{\mathrm{grid}} \leqslant \kappa_t^{\mathrm{grid}} \mathrm{P}_{\mathrm{rated}}^{\mathrm{TT}} \tag{12}$$

$$0 \leqslant P_{\mathrm{sell},t}^{\mathrm{grid}} \leqslant \left(1 - \kappa_t^{\mathrm{grid}}\right) \mathrm{P}_{\mathrm{rated}}^{\mathrm{TT}} \tag{13}$$

$$0 \leqslant P_{\mathrm{dis},t}^{\mathrm{bt}} \leqslant \kappa_t^{\mathrm{bt}} \mathrm{P}_{\mathrm{rate}}^{\mathrm{bt}} \tag{14}$$

$$0 \leqslant P_{\mathrm{ch},t}^{\mathrm{bt}} \leqslant \left(1 - \kappa_t^{\mathrm{bt}}\right) \mathrm{P}_{\mathrm{rate}}^{\mathrm{bt}} \tag{15}$$

$$0 \leqslant P_{\mathrm{dis},t}^{\mathrm{uc}} \leqslant \kappa_t^{\mathrm{uc}} \mathrm{P}_{\mathrm{rate}}^{\mathrm{uc}} \tag{16}$$

$$0 \leqslant P_{\mathrm{ch},t}^{\mathrm{uc}} \leqslant \left(1 - \kappa_t^{\mathrm{uc}}\right) \mathrm{P}_{\mathrm{rate}}^{\mathrm{uc}} \tag{17}$$

Constraint (3) denotes the PFC power difference between the α port and β port, depending on the charging/discharging power of HESS and PV output power, this ensures that power flows through the PFC in accordance with the net energy requirements of the system. Constraint (4) implies the active power balance between the power grid and FTPS. Constraint (5) defines the power supplied to the train through the β port converter (P_t^{TT}) and traction transformer ($P_{t,\beta}^{\mathrm{PFC}}$). It ensures that the required train power is met by the available sources. Constraints (6) and (7) state the energy profiles

in a battery or UC evolve time Δt, considering charging, discharging, and efficiency losses. Constraints (8) and (9) present the operational limits of the battery's and UC's energy storage capacity, ensuring that the stored energy E_t^{bt} remains within predefined minimum ($E_{\min}^{\text{bt}}, E_{\min}^{\text{uc}}$) and maximum ($E_{\max}^{\text{bt}}, E_{\max}^{\text{uc}}$) limits to prevent overcharging or deep discharging. Constraints (10) and (11) enforce periodic boundary conditions for the battery and UC energy storage. The initial energy $E_{\text{ini}}^{\text{bt}}$ and $E_{\text{ini}}^{\text{uc}}$ must match the final energy at $t = \text{T}$, ensuring a balanced cycle for energy storage over the planning horizon. Constraints (12) and (13) state the fact that purchasing power and selling power status cannot coexist simultaneously. The remaining constraints state that the charging and discharging power cannot exceed the rated power and capacity limits. They integrate binary decision variables $\kappa_t^{\text{grid}}, \kappa_t^{\text{bt}}, \kappa_t^{\text{uc}}$ to model state-dependent constraints, enabling precise control in the optimization framework. In addition, E_t^{bt} and E_t^{uc} denote the actual stored energy of the battery and UC, $P_{t,\text{cha}}^{\text{bt}}$ and $P_{t,\text{dis}}^{\text{bt}}$ represent the battery charging or discharging power, respectively. $P_{t,\text{cha}}^{\text{uc}}$ and $P_{t,\text{dis}}^{\text{uc}}$ represent the UC charging and discharging power, respectively. $\eta_{\text{cha}}^{\text{bt}}$ and $\eta_{\text{dis}}^{\text{bt}}$ represent the charging and discharging efficiency of the battery, while $\eta_{\text{cha}}^{\text{uc}}$ and $\eta_{\text{dis}}^{\text{uc}}$ represent the charging and discharging efficiency of the UC, respectively.

The mapping between the constraints described above and the compact matrix formulation in Problem 3.1 can now be clarified as follows. Specifically, Eqs. (12) - (17) indicate the coupling constraints for both $\boldsymbol{x}$ and $\boldsymbol{y}$, namely $\boldsymbol{Ax} + \boldsymbol{Dy} \leqslant \boldsymbol{f}$. Eqs. (8) and (9) represent the inequality constraints for $\boldsymbol{y}$, namely $\boldsymbol{By} \leqslant \boldsymbol{g}$. In contrast, Eqs. (3) -(7), (10) and (11) indicate the equality constraint, namely $\boldsymbol{Ey} = \boldsymbol{d}$.

3.2. Uncertainty Set of Train Load and PV

Based on the power flow prediction $[L_t, U_t]$ of traction load and PV output, a polyhedral uncertainty set $\mathcal{D}_{\text{P}}$ can be established controlled by the "budget of uncertainty" $\Gamma \in [0, \text{T}]$. Therefore, uncertainty sets associated with PV output and traction loads are denoted by $\mathcal{D}_{\text{P}}^{\text{tra}}$ and $\mathcal{D}_{\text{P}}^{\text{pv}}$, respectively:

$$\mathcal{D}_{\text{P}}^{\text{tra}} = \left\{ \boldsymbol{u}_{\text{tra}} \in \mathbb{R}^{+} \;\middle|\; \hat{P}_t^{\text{tra}} \in \left[\underbrace{P_t^{\text{tra}*} - e_t^{\text{tra}}}_{L_t}, \underbrace{P_t^{\text{tra}*} + e_t^{\text{tra}}}_{U_t} \right], \sum \frac{\left| \hat{P}_t^{\text{tra}} - P_t^{\text{tra}*} \right|}{e_t^{\text{tra}}} \leqslant \Gamma^{\text{tra}} \right\} \tag{18}$$

$$\mathcal{D}_{\text{P}}^{\text{pv}} = \left\{ \boldsymbol{u}_{\text{pv}} \in \mathbb{R}^{+} \;\middle|\; \hat{P}_t^{\text{pv}} \in \left[\underbrace{P_t^{\text{pv}*} - e_t^{\text{pv}}}_{L_t}, \underbrace{P_t^{\text{pv}*} + e_t^{\text{pv}}}_{U_t} \right], \sum \frac{\left| \hat{P}_t^{\text{pv}} - P_t^{\text{pv}*} \right|}{e_t^{\text{pv}}} \leqslant \Gamma^{\text{pv}} \right\} \tag{19}$$

where $P_t^{\text{tra}*}$ and $P_t^{\text{pv}*}$ represent the point forecast result based on the simulation toolbox [14],[30], e_t^{tra} and e_t^{pv} represent the forecast error under the different confidence level according to the historical data. Based on our previous work [14], a probabilistic prediction approach of traction load is proposed to capture the uncertainty of traction load. Similarly, the prediction approach of PV output can be found in [30].

Especially, expected-robustness parameters Γ^{tra} and Γ^{pv} are strategically set to balance the conservativeness of the optimal solution. For instance, setting Γ to 0 equates the power to the forecast at all times, representing a deterministic optimization model. As Γ increases from 0 to T, the size of the uncertainty set $\mathcal{D}_{\text{P}}$ also increases, indicating an expectation of larger deviations from the forecasted power. When Γ equals T, it suggests that the predicted power at each interval is highly uncertain, potentially reaching either the upper or lower bounds of the uncertainty set, and reflecting a condition of maximal uncertainty. A minimal budget of uncertainty may lead to violations of operational constraints and unsatisfactory objective values, indicating that the system lacks robustness against real-world uncertainties and risks. Conversely, an excessively large uncertainty budget is generally not advised, as it introduces a high level of conservativeness, potentially leading to escalated operating costs for the TSS.

3.3. Solution Methodology

The Min-Max-Min optimization problem, presented as Problem 3.1, is inherently non-convex and cannot be solved directly [31]. To address this issue, the KKT conditions and the theory of strong duality are utilized to reformulate the problem. The RO model is decomposed into a two-stage structure, where the outer-layer minimization ($\min_{\boldsymbol{x}}$) is defined as the Master Problem (MP), while the inner-layer Max-Min problem ($\max_{\boldsymbol{u} \in \mathcal{D}_{\text{P}}} \min_{\boldsymbol{y} \in \Omega(\boldsymbol{x}, \boldsymbol{u})}$) is converted into a convex maximization problem, serving as the Slave Problem (SP). This transformation reduces the original NP-hard problem to an equivalent two-stage mixed integer linear program (MILP).

3.3.1. Reformulation of Uncertainty Set (18) and (19)

Reference [32] has proved that there is a worst case when the traction load and PV output equal to its upper bound and lower bound respectively. Therefore, the uncertain set can be reformulated as a set described by binary variables $\kappa_t^{\text{tra}+}, \kappa_t^{\text{pv}-}$:

$$\mathcal{D}_{\text{P}}^{\text{tra}} = \left\{ \boldsymbol{u}_{\text{tra}} \in \mathbb{R}^{+} \;\middle|\; \begin{array}{c} \hat{P}_t^{\text{Tra}} = P_t^{\text{tra}*} + \kappa_t^{\text{tra}+} e_t^{\text{tra}} \\ \exists \kappa_t^{\text{tra}+} \in \{0, 1\} \\ \forall t, \sum_{t=1}^{\text{T}} \kappa_t^{\text{tra}+} \leqslant \Gamma^{\text{tra}} \end{array} \right\} \tag{20}$$

$$\mathcal{D}_{\text{P}}^{\text{pv}} = \left\{ \boldsymbol{u}_{\text{pv}} \in \mathbb{R}^{+} \;\middle|\; \begin{array}{c} \hat{P}_t^{\text{pv}} = P_t^{\text{pv}*} - \kappa_t^{\text{pv}-} e_t^{\text{pv}} \\ \exists \kappa_t^{\text{pv}-} \in \{0, 1\} \\ \forall t, \sum_{t=1}^{\text{T}} \kappa_t^{\text{pv}-} \leqslant \Gamma^{\text{pv}} \end{array} \right\} \tag{21}$$

3.3.2. *Reformulation of RO Problem 3.1*

The MP and SP could be obtained by decomposing Problem 3.1 as follow:

Problem 3.2 (Economic Dispatch Problem)**.**

$$\begin{aligned}
\textbf{MP}: \min_{\boldsymbol{x},\boldsymbol{y}} \quad & \varpi \\
\text{s.t.} \quad & \boldsymbol{x} \in \{0,1\},\ \varpi \geqslant \boldsymbol{\omega}^{\top}\boldsymbol{y} \\
& \Omega(\boldsymbol{x},\boldsymbol{u}) = \left\{ \boldsymbol{y} \;\middle|\; \begin{array}{l} \boldsymbol{A}\boldsymbol{x} + \boldsymbol{D}\boldsymbol{y} \leqslant \boldsymbol{f} \\ \boldsymbol{B}\boldsymbol{y} \leqslant \boldsymbol{g} \\ \boldsymbol{E}\boldsymbol{y} = \boldsymbol{d} \\ \boldsymbol{G}\boldsymbol{y} = \boldsymbol{u}^{\star}_{\text{tra}} \\ \boldsymbol{I}\boldsymbol{y} \leqslant \boldsymbol{u}^{\star}_{\text{pv}} \end{array} \right\}
\end{aligned}$$

where ϖ is the approximate estimate of objective function (1), $\boldsymbol{u}^{\star}_{\text{tra}}$ and $\boldsymbol{u}^{\star}_{\text{pv}}$ are the expected the worst scenario for the traction load set $\mathcal{D}^{\text{tra}}_{\text{P}}$ and PV output set $\mathcal{D}^{\text{pv}}_{\text{P}}$, determined by the Problem 3.3.

Problem 3.3 (Worst-case Decision Problem)**.**

$$\begin{aligned}
\textbf{SP}: \max_{\boldsymbol{u},\boldsymbol{\gamma}} \quad & \Big[-\left(\boldsymbol{f} - \boldsymbol{A}\boldsymbol{x}^{\star}\right)^{\top}\gamma_1 - \boldsymbol{g}^{\top}\gamma_2 + \boldsymbol{d}^{\top}\gamma_3 \\
& + \left(\gamma_4 P^{\text{tra}*}_t + e^{\text{tra}}_t \psi_t\right)^{\top}\gamma_4 - \left(\gamma_5 P^{\text{pv}*}_t - e^{\text{pv}}_t \mu_t\right)^{\top}\gamma_5 \Big] \\
\text{s.t.} \quad & -\boldsymbol{D}^{\top}\gamma_1 - \boldsymbol{B}^{\top}\gamma_2 + \boldsymbol{E}^{\top}\gamma_3 + \boldsymbol{G}^{\top}\gamma_4 - \boldsymbol{I}^{\top}\gamma_5 \leqslant \omega \\
& -\mathcal{M}\cdot\kappa^{\text{tra}+}_t \leqslant \psi_t \leqslant \mathcal{M}\cdot\kappa^{\text{tra}+}_t \\
& \gamma_4 - \mathcal{M}\left(1-\kappa^{\text{tra}+}_t\right) \leqslant \psi_t \leqslant \gamma_4 + \mathcal{M}\left(1-\kappa^{\text{tra}+}_t\right) \\
& 0 \leqslant \psi_t \leqslant \mathcal{M}\cdot\kappa^{\text{pv}-}_t \\
& \gamma_5 - \mathcal{M}\left(1-\kappa^{\text{pv}-}_t\right) \leqslant \mu_t \leqslant \gamma_5 \\
& \sum\nolimits_{t=1}^{\text{T}} \kappa^{\text{tra}+}_t \leqslant \Gamma^{\text{tra}} \\
& \sum\nolimits_{t=1}^{\text{T}} \kappa^{\text{pv}-}_t \leqslant \Gamma^{\text{pv}} \\
& \kappa^{\text{tra}+}_t, \kappa^{\text{pv}-}_t \in \{0,1\} \\
& \gamma_1, \gamma_2, \gamma_5 \geqslant 0 \\
& \gamma_3, \gamma_4 : \text{free}
\end{aligned}$$

where $\boldsymbol{x}^{\star}$ is the solving result of the Problem 3.2, γ_1, γ_2, γ_3, γ_4 and γ_5 denote the dual variables for constraint $\Omega(\boldsymbol{x},\boldsymbol{u})$.

3.3.3. *Standard Procedure*

The solving steps of the Column-and-Constraint Generation (C&CG) algorithm, a well-established algorithm for solving two-stage adjustable robust optimization problems, are outlined in Fig. 3. The specific steps are as follows:

1. Initialization: Start with an empty or relaxed MP. Set $LB = -\infty$ and $UB = +\infty$.
2. Solve the MP: Solve MP 3.2 with the current constraints and variables. Update LB using the optimal value.

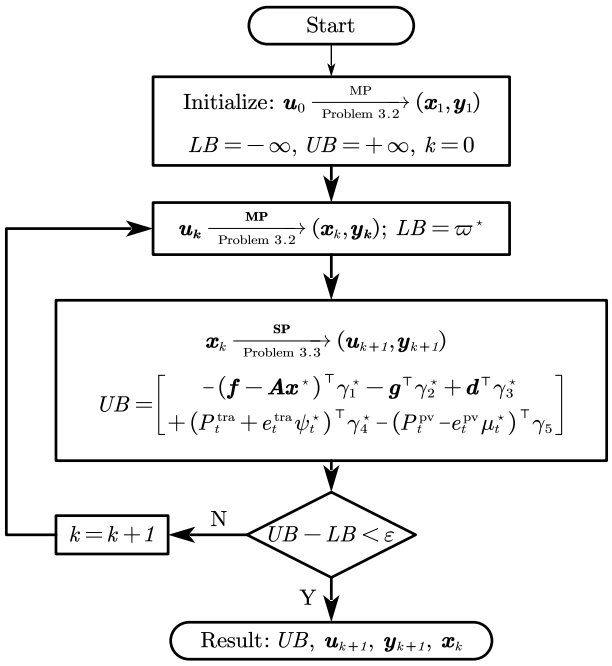

Figure 3: C&CG Algorithm.

3. Solve the SP: Solve SP 3.3 to find the most violating constraints or columns under the worst-case scenario. Update UB based on the optimal solution.
4. Convergence Check: If $UB - LB \leq \varepsilon$, terminate and output the solution. Otherwise, continue.
5. Generate Cuts: Add new constraints or variables ("cuts") from the SP to the MP and iterate.

4. R-EMS Control: Data-driven Adaptive Predictive Control

4.1. Reactive Power Compensation Problem Statement

Unlike high-speed trains, heavy-duty electric locomotives, such as the CEA1A with a rated power of 30 MW compared to the CR400AF's 20 MW, have a lower power factor and higher power demand. Additionally, heavy-haul railway TSS in China are typically connected to a 110 kV power system, rather than the 220 kV or higher voltage transmission networks used in high-speed rail. As a result, voltage imbalance and reactive power issues are more pronounced in heavy-haul railways than in high-speed rail systems.

4.1.1. *Power Quality Compensation Targets*

1) Target 1: Voltage Unbalance: The voltage unbalance factor (VUF) is dependent on the negative sequence current of TSS, short-circuit capacity (S_{PCC}) and rated voltage (U_{PCC}) of point of common coupling, which is defined as:

$$VUF = \frac{100\sqrt{3}U_{\text{PCC}}\left|\boldsymbol{I}^{-}_{\text{grid}}\right|}{S_{\text{PCC}}} \tag{22}$$

According to the voltage unbalance (VU) limit standard, such as IEC 61000-3-13, the unit of VU factor cannot exceed 2%. Thus, the VUF compensation target (VUF^*_{ref}) can set as:

$$I^-_{\text{ref}} = \frac{S_{\text{PCC}} \cdot VUF^*_{\text{ref}}}{100\sqrt{3}U_{\text{PCC}}} e^{j(\psi_L - \varphi_L)} \tag{23}$$

2) Target 2: Power Factor: Considering the reactive power of F-TSS, the power balance of constraint (4) can be supplemented with a reactive power balance constraint, namely $Q_t^{\text{TT}} + Q_{t,\alpha}^{\text{PFC}} = Q_t^{\text{grid}}$. Thus, the power factor of F-TSS can be expressed as:

$$PF = \frac{P_t^{\text{TT}} + P_{t,\alpha}^{\text{PFC}}}{\sqrt{\left(Q_t^{\text{TT}} + Q_{t,\alpha}^{\text{PFC}}\right)^2 + \left(P_t^{\text{TT}} + P_{t,\alpha}^{\text{PFC}}\right)^2}} \tag{24}$$

The active power and reactive power formulations of the traction transformer and PFC branch can be expressed using current and voltage products. Based on the instantaneous power theory, the current can be separated into instantaneous active/reactive power components, namely $I_{t,\text{p}}^{\text{TT}}$, $I_{t,\text{q}}^{\text{TT}}$, $I_{t,\alpha,\text{p}}^{\text{PFC}}$, $I_{t,\alpha,\text{q}}^{\text{PFC}}$, $I_{t,\beta,\text{p}}^{\text{PFC}}$, $I_{t,\beta,\text{q}}^{\text{PFC}}$. As a result, reactive power compensation can be achieved by compensating the reactive component in the current of the PFC branch ($I_{t,\alpha,\text{q}}^{\text{PFC}}$, $I_{t,\beta,\text{q}}^{\text{PFC}}$). For example, the power factor can not less than 0.9 based on the power quality standard in China.

4.1.2. Power Quality Compensation Strategy

Based on our previous research [33], given the VU target VUF^*_{ref} and power factor target PF^*_{ref}, the power quality compensation (PQC) current for each branch is given as:

$$\begin{bmatrix} I_{t,\alpha,\text{p}}^{\text{PFC}} \\ I_{t,\alpha,\text{q}}^{\text{PFC}} \\ I_{t,\beta,\text{p}}^{\text{PFC}} \\ I_{t,\beta,\text{q}}^{\text{PFC}} \end{bmatrix} = \begin{bmatrix} \frac{K_T}{K_\alpha} & 0 & -\frac{K_T}{K_\alpha} & 0 \\ 0 & \frac{K_T}{K_\alpha}\sqrt{\frac{1-PF^{*2}_{\text{ref}}}{PF^{*2}_{\text{ref}}}} & 0 & -\frac{K_T}{K_\alpha} \\ 1 & 0 & -1 & 0 \\ 0 & 1 & 0 & -1 \end{bmatrix} \begin{bmatrix} I_{t,\text{p}}^{\text{train}} \\ I_{t,\text{q}}^{\text{train}} \\ I_{t,\text{p}}^{\text{TT}} \\ I_{t,\text{q}}^{\text{TT}} \end{bmatrix} \tag{25}$$

$$\begin{bmatrix} I_{t,\text{p}}^{\text{TT}} \\ I_{t,\text{q}}^{\text{TT}} \end{bmatrix} = \frac{1}{t_1^2 + t_2^2} \begin{bmatrix} t_1 & t_2 \\ -t_2 & t_1 \end{bmatrix} \begin{bmatrix} t_3 \\ t_4 \end{bmatrix} \tag{26}$$

Notice, the terms t_1, t_2, t_3, t_4 is defined as:

$$\begin{bmatrix} t_1 \\ t_2 \end{bmatrix} = \frac{1}{3} K_T \begin{bmatrix} \cos(2\psi_T) - \cos(2\psi_\alpha) \\ \sin(2\psi_T) - \sin(2\psi_\alpha) \end{bmatrix} \tag{27a}$$

$$\begin{bmatrix} t_3 \\ t_4 \end{bmatrix} = \frac{S_{\text{PCC}} \cdot VUF^*_{\text{ref}}}{100\sqrt{3}U_{\text{PCC}}} \begin{bmatrix} \cos(2\psi_L - \varphi_L) \\ \sin(2\psi_L - \varphi_L) \end{bmatrix} - \frac{1}{3}\frac{K_T}{PF^*_{\text{ref}}} \begin{bmatrix} PF^*_{\text{ref}} \cdot \cos(2\psi_\alpha) + \sin(2\psi_\alpha) \\ PF^*_{\text{ref}} \cdot \sin(2\psi_\alpha) - \cos(2\psi_\alpha) \end{bmatrix} \tag{27b}$$

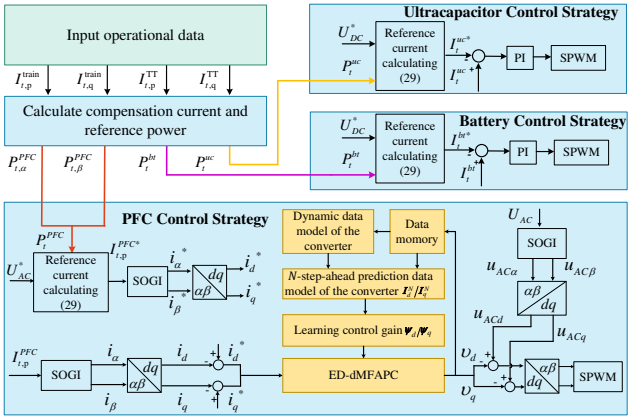

Figure 4: The control strategy of FTPS.

4.2. Real-time Control Strategy for PFC and ES Converters

Since the proposed FTPS consists of multiple converters, coordinated control for these converters is critical. For specified load conditions, power references are generated by the proposed robust optimisation approach. These references are then sent to the respective converters' controllers for power/current tracking, as illustrated in Fig. 4. Meanwhile, the power quality compensation strategy is embedded in the reference current based on the real-time voltage quality of FTPS.

As shown in Fig. 4, the adjusted reference power of the PFC and the energy storage is transmitted to the converter that executes the commands, the ultracapacitor and the battery use constant power control to track the adjusted reference power, and the single-phase back-to-back converter uses the ED-dMFAPC to adjust the output power according to the real-time power command of the substation while maintaining the voltage of the traction network.

According to Eqs. (3) and (25), the active power of the port satisfies the as follows:

$$U^*_{ACβ} I^{PFC}_{t,β,\text{p}} = U^*_{ACα} I^{PFC}_{t,α,\text{p}} + U^*_{DC}\left(I_t^{\text{PV}} + I_t^{bt} + I_t^{\text{uc}}\right) \tag{28}$$

The reference power that meets the power quality requirements is sent to the converter in real time, and the reference current of the converter can be derived as

$$\begin{bmatrix} I^{PFC}_{t,β,\text{p}} \\ I^{PFC}_{t,α,\text{p}} \\ I_t^{\text{PV}} \\ I_t^{bt} \\ I_t^{\text{uc}} \end{bmatrix} = \begin{bmatrix} \frac{1}{U^*_{ACβ}} & 0 & 0 & 0 & 0 \\ 0 & \frac{1}{U^*_{ACα}} & 0 & 0 & 0 \\ 0 & 0 & \frac{1}{U^*_{DC}} & 0 & 0 \\ 0 & 0 & 0 & \frac{1}{U^*_{DC}} & 0 \\ 0 & 0 & 0 & 0 & \frac{1}{U^*_{DC}} \end{bmatrix} \begin{bmatrix} P^*_{ACβ} \\ P^*_{ACα} \\ P_t^{\text{PV}} \\ P_t^{bt} \\ P_t^{\text{uc}} \end{bmatrix} \tag{29}$$

where $P^*_{ACα}$, $P^*_{ACβ}$, P_t^{PV}, P_t^{bt} and P_t^{uc} denote the reference power of PFC port $α$, PFC port $β$, PV, battery, and ultracapacitor.

$$\begin{bmatrix} u_d \\ u_q \end{bmatrix} = \begin{bmatrix} \cos(\omega t) & \sin(\omega t) \\ -\sin(\omega t) & \cos(\omega t) \end{bmatrix} \begin{bmatrix} u_\alpha \\ u_\beta \end{bmatrix} \tag{30a}$$

$$\begin{bmatrix} i_d^* \\ i_q^* \end{bmatrix} = \begin{bmatrix} \cos(\omega t) & \sin(\omega t) \\ -\sin(\omega t) & \cos(\omega t) \end{bmatrix} \begin{bmatrix} i_\alpha^* \\ i_\beta^* \end{bmatrix} \tag{30b}$$

where u_d, u_q, i_d, i_q represent the voltage and current of the $d-q$ coordinate axis, u_α, u_β, i_α, i_β represent the voltage and current after clark transformation, ωt represents the tracking angle of the phase-locked loop. Meanwhile, the control variables in the dMFAPC scheme refer to the i_d and i_q.

4.3. Direct Model-Free Adaptive Predictive Controller Design

The converter controller should rapidly and precisely track the reference signals i_d^*, i_q^*. To ensure stable and efficient control performance of current components i_d, i_q in α and β phases, this work investigates the dMFAPC for the converter.

The investigated converter control system is described as

$$\begin{aligned} i_x(t+1) = F_x\big(&i_x(t), i_x(t-1), \cdots, i_x\left(t-n_{1,x}\right), \\ &v_x(t), v_x(t-1), \cdots, v_x\left(t-n_{2,x}\right)\big) \end{aligned} \tag{31}$$

where x denotes the d-axis and q-axis, $F_x(\cdot)$ represents an unknown nonlinear function, i_x denotes the current components in α and β phases, v_x denote the control input in α and β phases, and $n_{1,x}$, $n_{2,x}$ are unknown system orders.

Develop a dynamic data model that is equivalent to the converter control system in Eq. (31) under rational assumptions [27]:

$$i_x(t+1) = i_x(t) + \phi_x(t)\,\Delta v_x(t) \tag{32}$$

where $\phi_x(t)$ is a time-varying parameter called pseudo partial derivative (PPD) with $|\phi_x(t)| \le b$, and $\Delta v_x(t) = v_x(t) - v_x(t-1)$.

Based on the data model in Eq. (32), the N-step-ahead prediction of current components can be derived as:

$$\boldsymbol{I}_x^N(t+1) = \boldsymbol{G} i_x(t) + \boldsymbol{\Phi}_x(t)\,\Delta \boldsymbol{V}_x^N(t) \tag{33}$$

where N denotes the prediction step size, $\boldsymbol{G} = [1, \cdots, 1]^{\mathrm{T}}$, $\boldsymbol{I}_x^N(t+1) = \left[i_x(t+1), \cdots, i_x(t+N)\right]^{\mathrm{T}}$ and $\boldsymbol{V}_x^N(t) = \left[v_x(t), \cdots, v_x(t+N)\right]^{\mathrm{T}}$ denote the N-step-ahead prediction vector of current component and control input, respectively, $\boldsymbol{\Phi}_x(t)$ denotes the pseudo partial derivative matrix, $\boldsymbol{\Phi}_x(t) =$

$$\begin{bmatrix} \phi_x(t) & 0 & 0 & 0 & 0 & 0 \\ \phi_x(t) & \phi_x(t+1) & 0 & 0 & 0 & 0 \\ \vdots & \vdots & \ddots & 0 & 0 & 0 \\ \phi_x(t) & \cdots & \cdots & \phi_x\left(t+N_u-1\right) & 0 & 0 \\ \vdots & \cdots & \cdots & \vdots & \ddots & 0 \\ \phi_x(t) & \phi_x(t+1) & \cdots & \phi_x\left(t+N_u-1\right) & \cdots & \phi_x(t+N-1) \end{bmatrix}$$

N_u denotes the control horizon constant, $\Delta \boldsymbol{V}_x^N(t) = \left[\Delta v_x(t), \cdots, \Delta v_x\left(t+N_u-1\right), \Delta v_x\left(t+N_u\right), \cdots, \Delta v_x(t+N-1)\right]^{\mathrm{T}}$, $\Delta v_x(t) = v_x(t) - v_x(t-1)$.

Theoretically, the converter control system is equipped with an ideal nonlinear predictive controller that ensures the asymptotic convergence of the currents i_d and i_q to their desired values. The ideal predictive controller is expressed as follows:

$$\boldsymbol{V}_x^N(t) = C_x\left(\bar{\boldsymbol{E}}_x^N(t+1)^{\mathrm{T}}, \bar{\boldsymbol{E}}_x^N(t)^{\mathrm{T}}, \cdots, \bar{\boldsymbol{E}}_x^N(t-m+2)^{\mathrm{T}}\right) \tag{34}$$

where $C_x(\cdot)$ denotes an unknown nonlinear function, m is an unkown controller order, $\bar{\boldsymbol{E}}_x^N(t-i) = \boldsymbol{I}_x^{N*}(t-i) - \boldsymbol{G} i_x(t-i)$, $i = -1, \cdots, m-2$.

Reasonable assumptions for Eq. (34) are given below.

Assumption 4.1. The partial derivative of $C_x(\cdot)$ over all its elements is continuous.

Assumption 4.2. $C_x(\cdot)$ satisfies the generalized Lipschitz condition. Specifically, if $\left\|\Delta \boldsymbol{\Theta}_x^N(t)\right\| \neq 0$, then it holds that $\left\|\Delta \boldsymbol{V}_x^N(t)\right\| \le c\left\|\Delta \boldsymbol{\Theta}_x^N(t)\right\|$, where $\Delta \boldsymbol{\Theta}_x^N(t) = \Big[-\bar{\boldsymbol{E}}_x^N(t)^{\mathrm{T}}, \Delta \bar{\boldsymbol{E}}_x^N(t)^{\mathrm{T}}, \cdots, \Delta \bar{\boldsymbol{E}}_x^N(t-L+2)^{\mathrm{T}}\Big]^{\mathrm{T}}$, L is pseudo controller order, $\Delta \bar{\boldsymbol{E}}_x^N(t-i) = \bar{\boldsymbol{E}}_x^N(t-i) - \bar{\boldsymbol{E}}_x^N(t-i-1)$, $i = 0, \cdots, L-2$, c is a positive constant.

Remark 4.1. For Assumption 4.1, the continuous derivative of $C_x(\cdot)$ with respect to system error is a typical condition for general nonlinear controllers. This condition is also a prerequisite for other data-driven control approaches, such as Virtual Reference Feedback Tuning (VRFT) [34] and Iterative Feedback Tuning (IFT) [35]. Assumption 4.2 limits the rate of change of the control input in relation to the system error, ensuring that the controller's energy remains finite when applied to a physical control plant with finite energy.

Theorem 4.1. For the ideal prediction controller given by (34), which satisfies Assumptions 4.1 and 4.2 with $\left\|\Delta \boldsymbol{\Theta}_x^N(t)\right\| \neq 0$, there exists a learning control gain $\boldsymbol{\psi}_x(t)$, such that (34) can be transformed into the following dMFAPC by employing the dynamic linearization technique.

$$\boldsymbol{V}_x^N(t) = \boldsymbol{V}_x^N(t-1) + \boldsymbol{\psi}_x(t)\,\Delta \boldsymbol{\Theta}_x^N(t) \tag{35}$$

where $\left\|\boldsymbol{\psi}_{\boldsymbol{x}}(t)\right\| \le c$, and $c > 0$ is an unknown constant.

Proof 4.1. See Theorem 1 in [36] for the similar detail.

Apply the first component of $\boldsymbol{V}_x^N(t)$ to the converter control system, and the control input is determined as:

$$v_x(t) = [1, 0, \cdots, 0]\,\boldsymbol{V}_x^N(t) \tag{36}$$

Remark 4.2. The proposed dMFAPC, featuring a simplified incremental form for converter control, is equivalent to the ideal controller. A key aspect of the controller design lies in the estimation of the learning control gain. While rapid control input actions lead to faster current tracking, they can also exacerbate overshoot, creating a trade-off between speed and stability within the framework.

4.4. Design of Learning Control Gain With Error Differential Characteristic for dMFAPC

To enhance the control performance and mitigate the contradiction, an adaptively learning control gain with error differential characteristic is proposed for dMFAPC for controlling of current components. The cost function considered

below incorporates the error differential characteristic and comprises three parts. The first parts minimizes the tracking error, the second penalizes rapid changes in the control input, and the third introduces an error differential term used to constrain the change rate in the tracking error.

$$J = \frac{1}{2}\left\|\boldsymbol{I}_x^{N*}(t+1) - \boldsymbol{I}_x^{N}(t+1)\right\|^2 + \frac{1}{2}\lambda\left\|\Delta\boldsymbol{V}_x^{N}(t)\right\|^2 + \frac{1}{2}\gamma\left\|\boldsymbol{I}_x^{N*}(t+1) - \boldsymbol{I}_x^{N}(t+1) - \boldsymbol{E}_x^{N}(t)\right\|^2 \tag{37}$$

where $\boldsymbol{I}_x^{N*}(t+1) = \left[i_x^*(t+1), \cdots, i_x^*(t+N)\right]^{\mathrm{T}}$ is the desired current vector, $\boldsymbol{E}_x^{N}(t) = \boldsymbol{I}_x^{N*}(t) - \boldsymbol{I}_x^{N}(t)$ is an current tracking error vector, λ and γ are positive constants.

Substituting the control law (35) into (37) and differentiating it with respect to the learning control gain $\boldsymbol{\psi}_x(t)$, it yields

$$\begin{aligned}\frac{\partial J}{\partial \boldsymbol{\psi}_x(t)} =& \\ -\frac{\partial \boldsymbol{I}_x^{N}(t+1)}{\partial \boldsymbol{V}_x^{N}(t)}&\left(\boldsymbol{I}_x^{N*}(t+1) - \boldsymbol{I}_x^{N}(t+1)\right)\Delta\bar{\boldsymbol{E}}_x^{N}(t)^{\mathrm{T}} \\ -\gamma\frac{\partial \boldsymbol{I}_x^{N}(t+1)}{\partial \boldsymbol{V}_x^{N}(t)}&\left(\boldsymbol{I}_x^{N*}(t+1) - \boldsymbol{I}_x^{N}(t+1) - \boldsymbol{E}_x^{N}(t)\right) \\ &\times\Delta\bar{\boldsymbol{E}}_x^{N}(t)^{\mathrm{T}} + \lambda\Delta\boldsymbol{V}_x^{N}(t)\,\Delta\bar{\boldsymbol{E}}_x^{N}(t)^{\mathrm{T}}\end{aligned} \tag{38}$$

Then, updating the learning control gain by gradient descent method

$$\boldsymbol{\psi}_x(t+1) = \boldsymbol{\psi}_x(t) - \eta\frac{\partial J}{\partial \boldsymbol{\psi}_x(t)} \tag{39}$$

where $\eta > 0$ is a learning rate.

To increase the flexibility of the updating law, following reset mechanism is given

$$\underline{\psi} \le \left\|\boldsymbol{\psi}_x(k)\right\| \le \bar{\psi} \tag{40}$$

For the N-step-ahead prediction of current $\boldsymbol{I}_x^{N}(t+1)$ in (38), it can be calculated through (33). Cost function for optimizing PPD parameters is given in (41)

$$J\left(\hat{\phi}_x(t)\right) = \left(\Delta i_x(t) - \hat{\phi}_x(t)\Delta v_x(t-1)\right)^2 + \mu\Delta\hat{\phi}_x(t) \tag{41}$$

Solving optimization problem for (41), by setting $\partial J\left(\hat{\phi}_x(t)\right)/\partial\hat{\phi}_x(t) = 0$, it yields

$$\hat{\phi}_x(t) = \hat{\phi}_x(t-1) + \frac{\sigma\left(\Delta i_x(t) - \hat{\phi}_x(t-1)\Delta v_x(t-1)\right)\Delta v_x(t-1)}{\mu + \Delta v_x(t-1)^2} \tag{42}$$

where $\sigma \in (0,1]$, $\mu > 0$, $\Delta i_x(t) = i_x(t) - i_x(t-1)$, $\Delta v_x(t-1) = v_x(t-1) - v_x(t-2)$.

The N-step PPD estimation algorithm is formulated based on an autoregressive model.

$$\begin{aligned}\hat{\phi}_x(t+j) = \omega_1(t)\hat{\phi}_x(t+j-1) + \omega_2(t)\hat{\phi}_x(t+j-2)& \\ + \cdots + \omega_n(t)\hat{\phi}_x(t+j-n)&\end{aligned} \tag{43}$$

where $j = 1, \cdots, N-1$.

Let $\boldsymbol{\omega}(t) = \left[\omega_1(t), \cdots, \omega_n(t)\right]^{\mathrm{T}}$, it is calculated as:

$$\boldsymbol{\omega}(t) = \boldsymbol{\omega}(t-1) + \frac{\hat{\boldsymbol{\varphi}}_{\boldsymbol{x}}(t-1)\left(\hat{\phi}_x(t) - \hat{\boldsymbol{\varphi}}_{\boldsymbol{x}}(t-1)^{\mathrm{T}}\boldsymbol{\omega}(t-1)\right)}{\delta + \left\|\hat{\boldsymbol{\varphi}}_{\boldsymbol{x}}(t-1)\right\|^2} \tag{44}$$

where $\hat{\boldsymbol{\varphi}}_{\boldsymbol{x}}(k-1) = \left[\hat{\phi}_x(k-1), \cdots, \hat{\phi}_x(k-n)\right]^{\mathrm{T}}$, n is a fixed model order, typically between 2 and 7, and $\delta \in (0,1]$.

To sum up, the ED-dMFAPC is composed of Eqs. (35), (36), (38)-(44).

Remark 4.3. The proposed converter controller is purely data-driven, eliminating the need for complex mathematical modeling. This makes it readily adaptable to practical applications after a few parameters being adjusted. L determines the memory length of the error data window used for controller synthesis and approximates the effective dynamic order of the controller. Typically, L is chosen empirically between 3-5.

5. Stability Analysis of R-EMS Control

Assumption 5.1. The sign of $\phi_x(t)$ remains invariant for all time t. Specifically, $\phi_x(t) > \epsilon > 0$ (or $\phi_x(t) < -\epsilon < 0$). Without loss of generality, this work adopts $\phi_x(t) > \epsilon > 0$.

Remark 5.1. Assumption 5.1 implies that the current changes in the same direction as the control input, indicating that the direction of control is predefined and consistent, which is the rational for the converter control system and is common in the model-based framework [37].

Theorem 5.1. For the converter control system described in Eq. (31) that satisfies Assumption 5.1, it is controlled by the proposed ED-dMFAPC in Eqs. (35),(36), (38)-(44), which complies with Assumptions 4.1 and 4.2. For the tracking problem, the current tracking error of the converter control system is guaranteed to be uniformly and ultimately bounded as long as condition $-2/b < \sum_{s=1}^{N}\psi_{x,1s}(t) < 0$ is met, i.e. $\lim_{t\to\infty} e_x(t+1) = \sqrt{\left(i_M + Z\right)^2/(1-\varrho)}$, $0 < \varrho < 1$, Z is defined in (48).

Proof 5.1. Define the current tracking error as $e_x(t) = i_x^*(t) - i(t)$, and compute the one-step ahead prediction tracking error.

$$\begin{aligned}&e_x(t+1) \\ &= i_x^*(t+1) - i_x(t+1) \\ &= \Delta i_x^*(t+1) + e_x(t) - [1,0,\cdots 0]\,\phi_x(t)\,\boldsymbol{\psi}_x(t)\,\Delta\boldsymbol{\Theta}_x^{N}(t) \\ &= \Delta i_x^*(t+1) + \left(1 + \phi_x(t)\sum_{s=1}^{N}\psi_{x,1s}(t)\right)e_x(t) \\ &\quad - \phi_x(t)\sum_{r=1}^{L-1}\sum_{s=rN+1}^{(r+1)N}\psi_{x,1s}(t)\Delta e_x(t-r+1)\end{aligned} \tag{45}$$

where the element $\psi_{x,1s}(t)$ represents the first row and the s-th column of the matrix $\boldsymbol{\psi}_x(t)$.

Define $\gamma(t) = -\phi_x(t) \sum_{r=1}^{L-1} \sum_{s=rN+1}^{(r+1)N} \psi_{x,1s}(t)\Delta e_x(t-r+1) + \Delta i_x^*(t+1)$. By utilizing the Lyapunov function $V(t+1) = e_x(t+1)^2$ and substituting (45) into it, we derive the first-order backward difference of $V(t+1)$

$$\begin{aligned}\Delta V(t+1) &= e_x(t+1)^2 - e_x(t)^2 \qquad (46)\\ &= \left[\left(1+\phi_x(t)\sum_{s=1}^{N}\psi_{x,1s}(t)\right)e_x(t)+\gamma(t)\right]^2 - e_x(t)^2\\ &\le \left(1+\phi_x(t)\sum_{s=1}^{N}\psi_{x,1s}(t)\right)^2 e_x(t)^2+\gamma(t)^2-e_x(t)^2\\ &= \left[\left(1+\phi_x(t)\sum_{s=1}^{N}\psi_{x,1s}(t)\right)^2-1\right]e_x(t)^2+\gamma(t)^2\end{aligned}$$

For practical applications, it is ensured that $|\Delta v(t)| \le v_M$ to prevent infinite variations in the control input, and $|\Delta i_x^*(t)| \le i_M$ is maintained to avoid abrupt changes in the desired current. According to the dynamic data model of converter control system (32), for the tracking problem, we have

$$\begin{aligned}|\Delta e(t)| &\le |\Delta i_x(t)| + |\Delta i_x^*(t)| \le |\phi_x(t-1)| \qquad (47)\\ &\times |\Delta v_x(t-1)| + |\Delta i_x^*(t)| \le b v_M + i_M\end{aligned}$$

For the seccond term on the right of $\gamma(t)$, $|\phi_x(t)| < b$ and $|\psi_{x,1s}(t)| \le \bar{\psi}$ given by Eq. (40), it follows that

$$\begin{aligned}|\phi_x(t)| \sum_{r=1}^{L-1}\sum_{s=rN+1}^{(r+1)N} |\psi_{x,1s}(t)|\,|\Delta e_x(t-r+1)| \le \qquad (48)\\ \bar{\psi}\left(b u_M + i_M\right)(L-1)N := Z\end{aligned}$$

With reference to Eq.(48), it has $|\gamma(t)| \le i_M + Z$. Employing Assumption 5.1 and the condition $-2/b < \sum_{s=1}^{N}\psi_{x,1s}(t) < 0$, further analysis from Eq. (46) leads to the subsequent result:

$$\begin{aligned}V(t+1) &\le \left(1+\phi_x(t)\sum_{s=1}^{N}\psi_{x,1s}(t)\right)^2 V(t) + \left(i_M+Z\right)^2\\ &\le \varrho V(t) + \left(i_M+Z\right)^2 \le \cdots \le \qquad (49)\\ &\le \varrho^t V(1) + \left(i_M+Z\right)^2\left(1-\varrho^{t-1}\right)/(1-\varrho)\end{aligned}$$

where $0 < \varrho < 1$.

With the definition of $V(t+1)$, it yields

$$\lim_{t\to\infty} e_x(t+1) = \sqrt{\left(i_M+Z\right)^2/(1-\varrho)} \qquad (50)$$

Hence, we can infer from Eq. (50) that the current tracking error is uniformly and ultimately bounded.

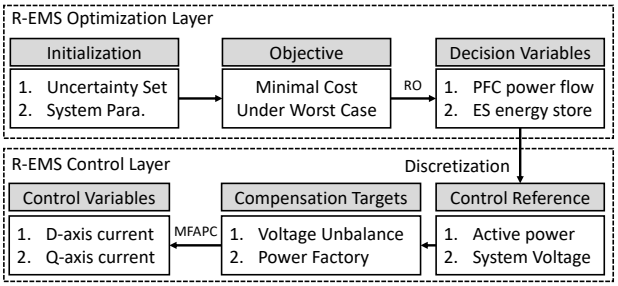

Figure 5: Optimization and simulation Process of R-EMS

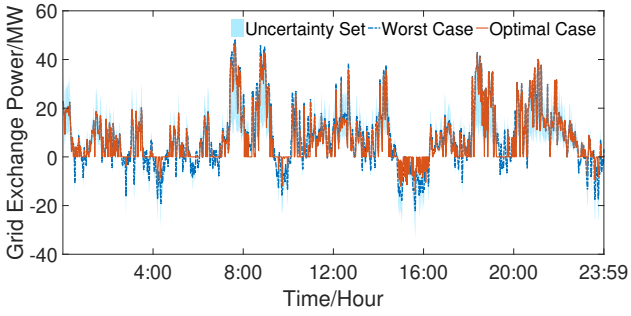

(a) Grid exchange power of F-TSS

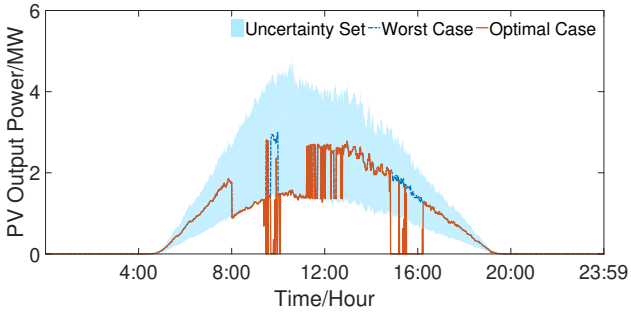

(b) PV output power

Figure 6: Day-ahead operation result of F-TSS under worst scenario

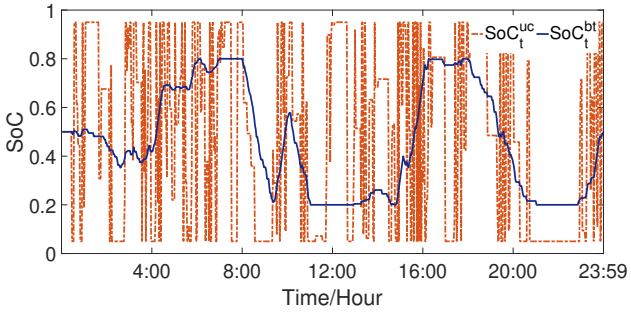

Figure 7: Day-ahead SoC of F-TSS

6. Case Studies

6.1. Setup

Fig. 5 shows the optimization and simulation process in the case studies. In the optimmziaiton layer, inputs include system design parameters, and confidence-based uncertainty sets, while the output of this stage includes optimal dispatch profiles for the battery, supercapacitor, and PFC unit. In the control layer, the controller tracks the dispatch targets

while simultaneously compensating for power quality issues such as voltage unbalance and reactive power deviation. The simulation outputs of the system include real-time control signals for energy storage, PFC converters, and the resulting TPSS voltage profile, which are used for performance evaluation in the case study.

The case studies use TSS field test data for an in-service heavy-haul railway in Shanxi, China. The studied F-TSS structure is illustrated in Fig. 1, while the robust real-time energy management framework is depicted in Fig. 2. The rated power of battery (P^{bt}_{rate}) and UC (P^{uc}_{rate}) are 8 MW and 10 MW, respectively, the rated capacity of battery and UC are 10 MWh and 0.1 MWh, respectively, other parameters η^{bt}_{cha}, η^{bt}_{dis}, η^{uc}_{cha} and η^{uc}_{dis} are from [16] and [19], respectively. The electrical prices are from [19]. To simulate PV output, the most recent annual solar irradiance data in the nearby area is obtained by [38]. The R-EMS optimization is solved by the robust optimization and the initial uncertainty parameters Γ^{tra}, Γ^{pv} are 200. The R-EMS control is performed by the power flow control and reactive power compensation with the model-free adaptive predictive controller. The robust optimization problem is solved by Gurobi 11.0.0 via YALMIP, while real-time control is implemented by MATLAB/SIMULINK. All simulations are performed on a workstation with an Intel(R) Core(TM) i5-13500 CPU and 64 GB RAM.

6.2. Performance of R-EMS Optimization

Fig. 6 (a) illustrates the grid exchange power between the power grid and the F-TSS. The light blue area represents the uncertainty region for traction power, while the navy blue dashed curve corresponds to the worst-case scenario determined by solving Problem 3.3. The results reveal a significant reduction in the peak-valley difference of the grid exchange power, demonstrating enhanced load balancing. Furthermore, approximately 79.15 % of the RBE represented as negative power, is effectively stored or utilized compared to the initial worst-case scenario. Fig. 6 (b) depicts the actual PV output power, showing that nearly all PV generation is directly consumed to meet the traction power demand, thereby reducing reliance on grid energy.

Fig. 7 depicts the SoC for the battery and the UC, respectively. The UC experiences frequent charging and discharging cycles, reflecting its role in accommodating rapid power fluctuations. The battery exhibits a more stable operation curve, underscoring its utility in meeting sustained energy demands over longer periods.

Fig. 8 (a) and (b) present the power balance within the F-TSS. The results indicate that the majority of RBE is efficiently stored in the battery ($P^{bt}_{t,cha}$) and ultracapacitor ($P^{uc}_{t,cha}$), with the stored energy later discharged to fulfill traction power demands. Notably, at 11:00, the F-TSS not only meets the entire traction power demand but also operates independently without drawing power from the grid. This highlights the system's ability to achieve grid-free operation during specific intervals. By integrating RBE and PV output, the proposed R-EMS optimization approach effectively

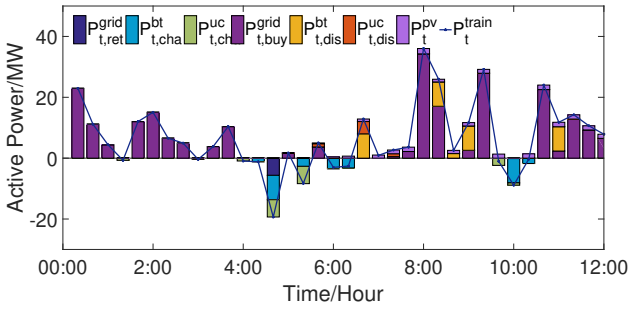

(a) 00:00 12:00

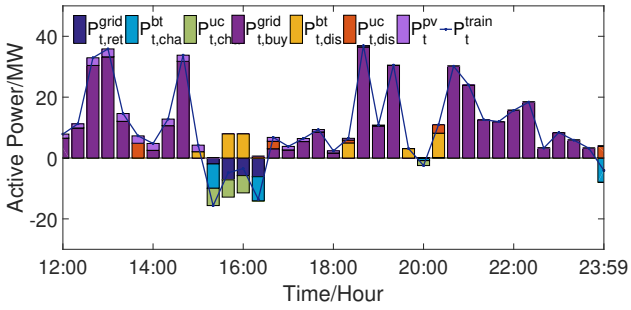

(b) 12:00 23:59

Figure 8: Power balance of F-TSS under the optimal day-ahead schedule.

Table 1
Total daily operation cost of F-TSS under the worst-case scenario ($\Gamma^{tra} = \Gamma^{pv} = 200$)

Cost items	Without Optimization	DO model	RO model
C^{ene}/k$	27.74	24.39	22.63
C^{dem}/k$	8.11	7.57	7.57
C^{HESS}/k$	-	0.75	0.85
Total cost/k$	35.85	32.71	31.05

minimizes energy waste and enhances grid stability. This integration enables the F-TSS to function as a dynamic and flexible node, improving energy efficiency and supporting the development of sustainable and resilient railway systems.

Fig. 9 highlights the significant changes in the PFC power curve before and after applying robust optimization. Under the same worst-case scenario, to address the uncertainties in traction load and PV power, the maximum transfer power of the PFC reaches 19.34 MW when using deterministic optimization (DO) as referenced in [13], [22]. However, after implementing the robust optimization approach, the maximum transfer power of the PFC is reduced by 29 % to 13.68 MW. This reduction demonstrates the ability of robust optimization to flexibly adjust energy flows and effectively mitigate peak power demands.

Table 1 presents the optimization results under the worst-case scenario. It shows that the daily total cost is reduced by 13.39 % (from 35.85 k$ to 31.05 k$) after applying the proposed R-EMS optimization approach for the F-TSS. Compared with DO model [13], [22], the energy

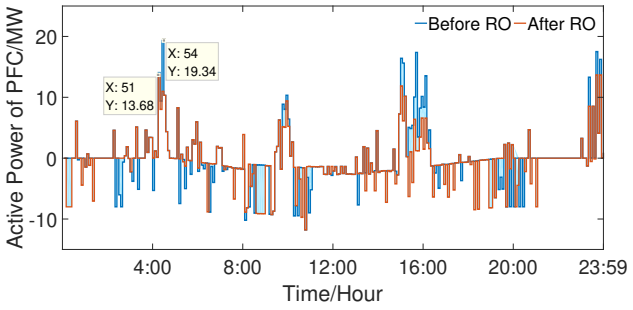

Figure 9: Changes in the power flow of PFC before and after RO in F-TSS.

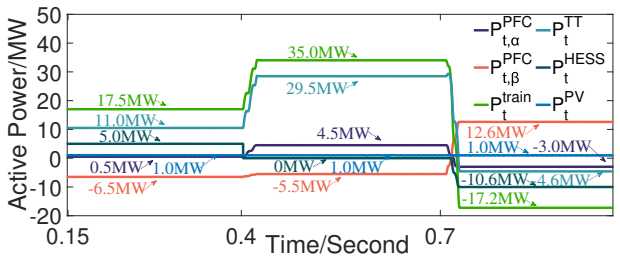

(a) Before power quality compensation

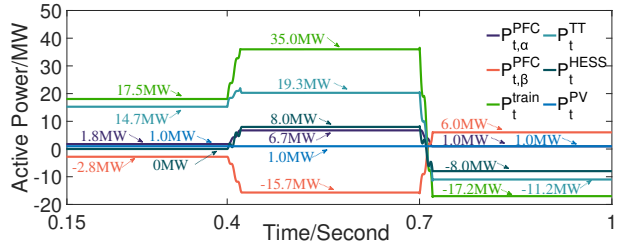

(b) After power quality compensation

Figure 10: Power curves for different operating conditions.

consumption contributes a reduction of 5.07 %. Consequently, the proposed day-ahead dispatch approach achieves a well-calibrated balance between robustness and economic efficiency, ensuring reliable operation.

6.3. Performance of R-EMS Control

Three typical operation scenarios were derived from Fig. 8 to assess the performance of the R-EMS control, including RBE utilization, maximum demand shaving, and power quality improvement. Figs. 10 (a) and (b) illustrate the power flow distribution across the F-TSS ports before and after power quality compensation. From 0.15s to 0.4s, the train operates in traction mode with a power consumption of 17.5 MW. After enabling power quality compensation, the energy storage system transitions to standby mode, and the power of the two PFC ports and the transformer port is adjusted to meet the required voltage unbalance factor (VUF) and power factor (PF) specifications. From 0.4s to 0.7s, the train operates at maximum traction mode, drawing 35 MW of power. With power quality compensation, the energy storage switches to discharging mode, achieving maximum demand shaving. Between 0.7s and 1.0s, during braking mode, the

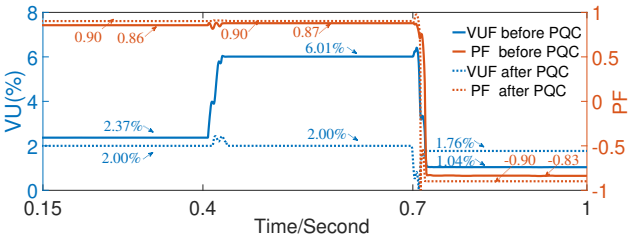

Figure 11: Power quality for different operating scenarios.

Table 2
Comparison of Different Control Schemes

	PID [20], [33]		dMFAPC	
	i_d	i_q	i_d	i_q
ISE	8579.7	3032.3	861.2	159.5
IAE	44.2	50.2	3.8	5.4

train generates 17.2 MW of RBE. The energy storage system absorbs the RBE, and any excess energy is returned to the utility grid.

Fig. 11 illustrates the power quality compensation performance. Between 0.15s and 0.7s, the traction load increases from 17.5 MW to 35.0 MW, while the VUF rises from 2.37 % to 6.01 %. After enabling power quality compensation, the VUF is effectively reduced to 2.00 %, meeting the IEC 61000-3-13 standard. Additionally, the power factor improves from 0.86 to 0.90. Between 0.7s and 1.0s, when the traction load decreases from 35.0 MW to -17.2 MW, both the VUF and power factor are well compensated. In summary, the proposed R-EMS control can achieve efficient RBE utilization, and power quality issue improvement.

Fig. 12 compares the tracking performance of the current components i_d and i_q between the proposed dMFAPC and the methods presented in [20] and [33]. The controller's performance is evaluated using two common indicators: the Integral of Squared Error (ISE) and the Integral of Absolute Error (IAE), which are detailed in Table 2. The ISE measures the accumulated squared deviation between the reference signal and the actual output, providing an indication of the overall accuracy of the tracking system. Lower ISE values indicate better performance with smaller deviations. The IAE, on the other hand, measures the total absolute deviation and is particularly useful for assessing the steady-state error over time. Smaller IAE values suggest that the system can quickly adapt to changes and maintain a closer tracking to the reference. Table 2 shows that the ISE improved by 89 % for the d-axis current and 94 % for the q-axis current, while the IAE improved by 91 % and 89 %, respectively. These results demonstrate that the dMFAPC significantly outperforms traditional PID control in tracking both i_d and i_q. The improvements in ISE and IAE highlight the superior control accuracy and dynamic response of the dMFAPC compared to conventional PID-based approaches.

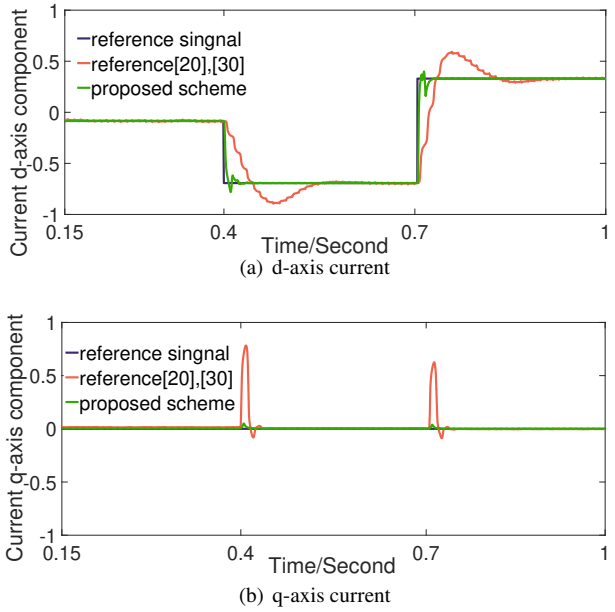

(a) d-axis current

(b) q-axis current

Figure 12: Comparison of the tracking performance of the dMFAPC and the control of reference [20], [33].

7. Conclusion

In this paper, a robust R-EMS framework for F-TSS in heavy-haul railways is proposed to against the uncertainty of freight train power demand and PV output. At the R-EMS optimization stage, a day-ahead robust optimization method effectively mitigates the impact of worst-case scenarios, ensuring resilient operation while maximizing energy-saving profits. At the R-EMS control stage, an ED-dMFAPC provides precise and rapid tracking of day-ahead scheduling plans while improving power quality through voltage unbalance mitigation and reactive power support. The results demonstrate that through optimizing the coordination of PFC and ES, the framework achieved a 13.39 % reduction in total operational costs and a significant improvement in the ISE and IAE, with reductions of at least 89 %. Consequently, the proposed R-EMS framework provides an effective solution for integrating renewable energy and managing uncertainties in heavy-haul railways. It offers a scalable and adaptable approach to optimizing energy management and control for F-TSS, contributing to more sustainable, cost-effective, and resilient railway TPSs. Future research could explore extending this framework to incorporate additional renewable energy sources and dynamic multi-substation coordination strategies.

CRediT authorship contribution statement

Bo Li: Conceptualization, Methodology, Writing – original draft. **Minwu Chen:** Conceptualization, Funding acquisition, Supervision, Resources. **Guowang Yu:** Investigation, Resources, Validation. **Chen Chen:** Methodology, Software, Writing – original draft. **Yinyu Chen:** Methodology, Software, Writing – original draft. **Kang Li:** Resources, Writing - Review & Editing.

Declaration of competing interest

The authors declare that they have no known competing financial interests or personal relationships that could have appeared to influence the work reported in this paper

Data availability

Data will be made available on request.

Acknowledgments

The research was supported by the National Natural Science Foundation of China [Grant No.52277126].

References

[1] I. H. H. Association, Heavy haul vision 2030, 2023. Accessed: 2025-01-16.

[2] X. Lin, Z. Liang, L. Shen, F. Zhao, X. Liu, P. Sun, T. Cao, Reinforcement learning method for the multi-objective speed trajectory optimization of a freight train, Control Engineering Practice 138 (2023) 105605.

[3] X. Tao, Q. Wang, M. Chen, P. Sun, X. Feng, Comprehensive optimization of energy consumption and network voltage stability of freight multi-train operation based on ammopso algorithm, IEEE Transactions on Transportation Electrification (2023).

[4] Z. Xiao, Q. Wang, P. Sun, B. You, X. Feng, Modeling and energy-optimal control for high-speed trains, IEEE Transactions on transportation electrification 6 (2020) 797–807.

[5] Z. Tian, N. Zhao, S. Hillmansen, C. Roberts, T. Dowens, C. Kerr, Smartdrive: Traction energy optimization and applications in rail systems, IEEE Transactions on Intelligent Transportation Systems 20 (2019) 2764–2773.

[6] Y. Cao, Z. Zhang, F. Cheng, S. Su, Trajectory optimization for high-speed trains via a mixed integer linear programming approach, IEEE Transactions on Intelligent Transportation Systems 23 (2022) 17666–17676.

[7] Z. Xiao, H. Chen, J. Guo, Q. Wang, P. Sun, X. Feng, Joint optimization of speed and voltage trajectories for hybrid electric trams, IEEE Transactions on Industry Applications 57 (2021) 6427–6439.

[8] N. D. Popovich, D. Rajagopal, E. Tasar, A. Phadke, Economic, environmental and grid-resilience benefits of converting diesel trains to battery-electric, Nature Energy 6 (2021) 1017–1025.

[9] K. Deng, H. Peng, S. Dirkes, J. Gottschalk, C. Ünlübayir, A. Thul, L. Löwenstein, S. Pischinger, K. Hameyer, An adaptive pmp-based model predictive energy management strategy for fuel cell hybrid railway vehicles, ETransportation 7 (2021) 100094.

[10] Z. Pan, M. Chen, S. Lu, Z. Tian, Y. Liu, Integrated timetable optimization for minimum total energy consumption of an ac railway system, IEEE Transactions on Vehicular Technology 69 (2020) 3641–3653.

[11] J. A. Aguado, A. J. S. Racero, S. de la Torre, Optimal operation of electric railways with renewable energy and electric storage systems, IEEE Transactions on Smart Grid 9 (2016) 993–1001.

[12] H. Novak, V. Lešić, M. Vašak, Hierarchical model predictive control for coordinated electric railway traction system energy management, IEEE Transactions on Intelligent Transportation Systems 20 (2018) 2715–2727.

[13] H. Dong, Z. Tian, J. W. Spencer, D. Fletcher, S. Hajiabady, Coordinated control strategy of railway multisource traction system

with energy storage and renewable energy, IEEE Transactions on Intelligent Transportation Systems 24 (2023) 15702–15713.
[14] Y. Chen, M. Chen, M. Cui, W. Lu, Y. Lv, Voltage unbalance probability pre-assessment of electrified railways with uncertain traction load, IEEE Transactions on Transportation Electrification 9 (2022) 1509–1520.
[15] X. Wang, Y. Han, L. Li, J. Wang, W. Chen, W. Shen, Cvar quantitative uncertainty-based optimal dispatch for flexible traction power supply system, IEEE Transactions on Transportation Electrification 10 (2023) 1900–1910.
[16] Y. Chen, M. Chen, L. Xu, Z. Liang, Chance-constrained optimization of storage and pfc capacity for railway electrical smart grids considering uncertain traction load, IEEE Transactions on Smart Grid 15 (2023) 286–298.
[17] G. Li, S. W. Or, Multi-agent deep reinforcement learning-based multi-time scale energy management of urban rail traction networks with distributed photovoltaic–regenerative braking hybrid energy storage systems, Journal of Cleaner Production (2024) 142842.
[18] L. Jiang, Z. Bie, T. Long, H. Xie, Y. Xiao, Distributed energy management of integrated electricity-thermal systems for high-speed railway traction grids and stations, CSEE Journal of Power and Energy Systems 7 (2020) 541–554.
[19] Y. Liu, M. Chen, Z. Cheng, Y. Chen, Q. Li, Robust energy management of high-speed railway co-phase traction substation with uncertain pv generation and traction load, IEEE Transactions on Intelligent Transportation Systems 23 (2021) 5079–5091.
[20] Y. Ge, H. Hu, J. Chen, K. Wang, Z. He, Hierarchical energy management of networked flexible traction substations for efficient rbe and pv energy utilization within ers, IEEE Transactions on Sustainable Energy 14 (2023) 1397–1410.
[21] P. Guo, Z. Tian, Z. Yuan, X.-Y. Zhang, D. Sharifi, Research on symmetric bipolar mmc-m 2 tdc-based flexible railway traction power supply system, IEEE Transactions on Transportation Electrification 10 (2023) 1043–1055.
[22] X. Wang, Q. Guo, C. Tu, L. Wang, F. Xiao, J. Luo, Y. Hou, A novel hybrid advanced cophase power supply equipment with its operation control strategy, IEEE Transactions on Industrial Electronics (2024).
[23] Q. Guo, X. Wang, C. Tu, L. Che, F. Xiao, Y. Hou, A multi-timescale energy management strategy for advanced cophase traction power supply system with pv and es, IEEE Transactions on Transportation Electrification (2024).
[24] X. Meng, Q. Zhang, G. Hu, G. Zhang, Y. Zhang, F. Liu, Z. Liu, Multi-vehicle accessed railway vehicle-grid system stability analysis and optimization based on oltc, Control Engineering Practice 141 (2023) 105693.
[25] Z. Xu, L. Pan, T. Shen, Model-free reinforcement learning approach to optimal speed control of combustion engines in start-up mode, Control Engineering Practice 111 (2021) 104791.
[26] D. Zhao, S. Gao, F. Li, X. Yan, S. K. Spurgeon, Model-free adaptive tensor product control for a class of nonlinear systems, Control Engineering Practice 147 (2024) 105912.
[27] Z. Hou, S. Jin, Model free adaptive control: Theory and applications, CRC Press, 2013.
[28] Y. Guo, Z. Hou, S. Liu, S. Jin, Data-driven model-free adaptive predictive control for a class of mimo nonlinear discrete-time systems with stability analysis, IEEE Access 7 (2019) 102852–102866.
[29] F. Li, Z. Hou, Event-triggered model-free adaptive predictive control for networked control systems under deception attacks, IEEE Transactions on Systems, Man, and Cybernetics: Systems (2023).
[30] Y. Shi, N. Chen, Conditional kernel density estimation considering autocorrelation for renewable energy probabilistic modeling, IEEE Transactions on Power Systems 36 (2020) 2957–2965.
[31] H. Qiu, B. Zhao, W. Gu, R. Bo, Bi-level two-stage robust optimal scheduling for ac/dc hybrid multi-microgrids, IEEE Transactions on Smart Grid 9 (2018) 5455–5466.
[32] D. Bertsimas, E. Litvinov, X. A. Sun, J. Zhao, T. Zheng, Adaptive robust optimization for the security constrained unit commitment problem, IEEE transactions on power systems 28 (2012) 52–63.
[33] M. Chen, Y. Chen, Y. Chen, X. Dai, L. Liu, Unified power quality management for traction substation groups connected to weak power grids, IEEE Transactions on Power Delivery 37 (2022) 4178–4189.
[34] S. Formentin, M. C. Campi, A. Carè, S. M. Savaresi, Deterministic continuous-time virtual reference feedback tuning (vrft) with application to pid design, Systems & Control Letters 127 (2019) 25–34.
[35] M. F. Heertjes, B. Van der Velden, T. Oomen, Constrained iterative feedback tuning for robust control of a wafer stage system, IEEE transactions on control systems technology 24 (2015) 56–66.
[36] X. Yu, Z. Hou, M. M. Polycarpou, A data-driven ilc framework for a class of nonlinear discrete-time systems, IEEE Transactions on Cybernetics 52 (2021) 6143–6157.
[37] Z. Hou, S. Xiong, On model-free adaptive control and its stability analysis, IEEE Transactions on Automatic Control 64 (2019) 4555–4569.
[38] M. Sengupta, Y. Xie, A. Lopez, A. Habte, G. Maclaurin, J. Shelby, The national solar radiation data base (nsrdb), Renewable and sustainable energy reviews 89 (2018) 51–60.